Chemical Engineering Journal 419 (2021) 129660

Contents lists available at ScienceDirect

Chemical Engineering Journal

journal homepage: www.elsevier.com/locate/cej

Graphene confined intermetallic magnesium silicide nanocrystals with highly exposed (220) facets for anisotropic lithium storage

Baoping Zhang [a,b], Qinfen Gu [c], Hongyu Zhang [a], Xuebin Yu [a,*]

[a] Department of Materials Science, Fudan University, Shanghai 200433, China
[b] Department of Mechanical Engineering, City University of Hong Kong, Hong Kong, China
[c] Australian Synchrotron (ANSTO), 800 Blackburn Road, Clayton 3168, Australia

ARTICLE INFO

Keywords:
Magnesium silicide
Magnesium hydrides
Hydrogen driven
Li-ions migration path
Anisotropic lithium storage

ABSTRACT

Intermetallic Magnesium silicide (Mg_2Si) is regarded as a promising electrode material for lithium-ion batteries (LIBs), by virtue of its desirable electrochemical activity, high theoretical capacity, suitable voltage profiles, and lightweight. Nevertheless, its practical application is still hindered by poor electrochemical kinetics and rapid capacity fading. Herein, high-purity intermetallic Mg_2Si nanocrystals (NCs) encapsulated by graphene-layer matrix (Mg_2Si@G) are designed for advanced lithium storage. The graphene-confined Mg_2Si NCs, featuring with high-purity, highly exposed (220) facets and nanopores, are fabricated *via* a facile hydrogen-driven silicification and subsequent freeze-drying process. Combined DFT calculations and experimental studies illustrate an anisotropic lithium storage of Mg_2Si, exhibiting rapid Li-ions migration path along exposed (220) facets and highly reversible solid solution behavior. Benefiting from the desirable structure features and interactions, Mg_2Si@G ensures a spatially confined (de)lithiation with high electrochemical activity and fast electronic/ionic transport kinetics, leading to largely enhanced lithium storage performance. The resulting Mg_2Si@G electrode delivers a high capacity (100th capacity of 831 mAh g^{-1} at 100 mA g^{-1}), outstanding rate capability and long-term cycle stability (3000th capacity of 578 mAh g^{-1} at 2 A g^{-1}). This work presents a new perspective towards the rational development of well-performing Mg_2Si materials for lithium storage.

1. Introduction

To satisfy the ever-increasing demands on the high density of rechargeable lithium-ion batteries (LIBs), constant efforts have been devoted to the exploit of next generation well-performing novel electrode materials in the past two decades [1–3]. In this context, a variety of potential candidates based on metals or semiconductors compounds (metal oxides, sulfides, carbides, nitrides, phosphides, hydrides, etc.) have been intensively studied because of their high theoretical capacities outweighing that of the commercial graphite (372 mAh g^{-1}) [4–12]. Among them, intermetallic compounds, which possess intermediate properties between metallic and non-metallic materials, have provided a new perspective for high-performance lithium storage. Particularly, in the early 1990s, Huggins et al. [13] pioneeringly proposed the new concept of using Si-based intermetallic (Si-M, M = Mg, Ca, Mo, etc.) as electrode materials for LIBs. These Si-M intermetallic materials have shown much better electrochemical performances than silicon alone, due to the desirable thermodynamic properties, enhanced electronic conductivities, and the active/inactive matrix roles for buffering the volumetric expansion upon lithium insertion. To this end, various favorable Si-M intermetallic, e.g., Ni_2Si [14–16], $FeSi_2$ [17,18], Ti_2Si [19,20], $MoSi_2$ [21–23] and Ca_2Si [24,25] have sprung up for high-performance lithium storage.

Among the myriad of metal silicide, intermetallic magnesium silicide (Mg_2Si) is regarded as one of the most attractive candidates for LIBs, by virtue of its anti-fluorite type structure for reversible lithium storage, high potential theoretical capacity (higher than 1398 mAh g^{-1}, 4 Li insertion), the appropriately low and flat voltage profiles ($\leq$0.5 V *vs.* Li/Li^+) comparable to graphite anode, and lightweight (1.99 g cm^{-3}). Moreover, the raw materials of magnesium and silicon resource of Mg_2Si are natural abundant, eco-friendly and low cost, which could provide great potential for industrial application. In spite of above competitive and attractive advantages, nevertheless, the progress of Mg_2Si electrode is still largely hindered by the rapid capacity fading and poor electrochemical kinetics, especially in forms of the bulk state. For instance, the discharge capacity of Mg_2Si electrode at 10 mA g^{-1} decreases

* Corresponding author.
E-mail address: yuxuebin@fudan.edu.cn (X. Yu).

https://doi.org/10.1016/j.cej.2021.129660
Received 4 January 2021; Received in revised form 21 February 2021; Accepted 31 March 2021
Available online 7 April 2021

dramatically from nearly 1384 mAh g^{-1} to less than 200 mAh g^{-1} within ten cycles [26,27]. The inferior performances are mainly ascribed to the poor electronic conductivity, slow Li-ions diffusion rate, and volumetric effect upon deep cycling. Worse, Mg_2Si electrode proceeds multi-steps structural expansion-shrinkage-expansion variation solely during lithiation process, leading to server structural instability. The losing of active nanograins upon cycling due to its easily self-growth and agglomeration, would finally lead to poor reversibility and thus fast capacity fading [28].

To address these issues, constant efforts have been made to optimize the performance of Mg_2Si electrodes by favourble structural design and fabrication, such as rational nanostructured strategies, carbon coating and compositing, and pre-lithiation or alloying assisted [26,29–37]. Among these efforts, the nanostructure techniques have been widely reported to be efficient strategies to enhance the electrochemical kinetics and alleviate the volumetric strain of electrode materials during cycling. However, due to the inert silicon and high reactivity of Mg_2Si, the development of feasible techniques for fabricating nanostructured Mg_2Si materials with high purity and in a controlled manner remains a great challenge [38–41]. For instance, Tamirat et al. [32] fabricated a carbon coated Mg_2Si by a thermal vapor deposition technique, which exhibits an attractive rate performance with a 500th cycle capacity of 380 mAh g^{-1} at a current density of 2 A g^{-1}. However, the fabrication is complex and high-energy consumable, which also brought out inevitable oxidation using Mg and Si as the starting materials. Besides, Liu et al. [41] proposed a much gentle hydrogen-driven chemical reaction technique based on metal hydrides, and the resulting Mg_2Si electrodes exhibit a high initial discharge capacity (1095 mAh g^{-1}) with 37% capacity retains over 60 cycles. In spite of these favorable enhancements, the lithium storage performance of Mg_2Si electrodes are still far from being satisfactory.

Besides the sizes and crystal structures, the crystallographic plane orientation also effects the lithium storage behavior. Tailoring a particularly exposed crystal planes is another effective way to achieve high-rate capability for LIBs [42,43]. However, few reports have illustrated the characteristic surface crystal planes of Mg_2Si and its effects on the electrochemical behavior. Inspired by these concepts, it is highly desirable to design rational Mg_2Si materials with desirable morphologies and crystal structure with particularly highly exposure channel for Li-ions diffusion, so as to unlock its electrochemical performances for LIBs.

In this study, high-purified intermetallic Mg_2Si NCs (an average size of 50 nm) decorated with nanopores and highly exposed (220) facets, have been prepared through a facile hydrogen-driven reaction strategy. The Mg_2Si NCs were further encapsulated by graphene-layer matrix through a freeze-drying process to get efficient electron conduction and spatially confinement. Combined DFT calculation and experimental studies illustrate the rapid Li-ions migration path along highly exposed (220) facets and efficient solid solution behavior with high reversibility, indicating an anisotropic surface lithium storage. Taking advantaging of the desirable interactions between Mg_2Si NCs and graphene, the Mg_2Si@G electrode was endowed with superior electrochemical activity, fast electronic/ionic transport kinetics, and spatially confined (de) lithiation process, leading to largely enhanced lithium storage performances, in terms of outstanding capacity, rate capability, and cycling stability.

2. Results and discussions

2.1. Structure of Mg_2Si@G with highly exposed (220) facets

Fig. 1a displays the synthetic process of Mg_2Si@G. We introduce a facile Silicon templated hydrogen-driven silicification for the fabrication of Mg_2Si NCs. Typically, Mg_2Si NCs were prepared using Silicon NCs (Fig. 1b) and MgH_2 as the starting materials *via* a hydrogen(H)-driven reaction: 2 MgH_2 (s) + Si (s) → Mg_2Si (s) + 2 H_2 (g). The pre-activate treatment of reactants by ball milling (Fig. 1c) and the dehydrogenation process of MgH_2 is largely beneficial for the complete conversion reaction at lower temperature (450 °C). The dehydrogenation of MgH_2 and the lattice orientation rearrangement during silicification finally give rise to the growth of Mg_2Si NCs (Fig. 1d), featured with high purity, an average size of 50 nm with nanopores and highly exposed (220) facets, which would be illustrated in the later paragraphs. Subsequently, Mg_2Si NCs can be well encapsulated by the flexible graphene-layer

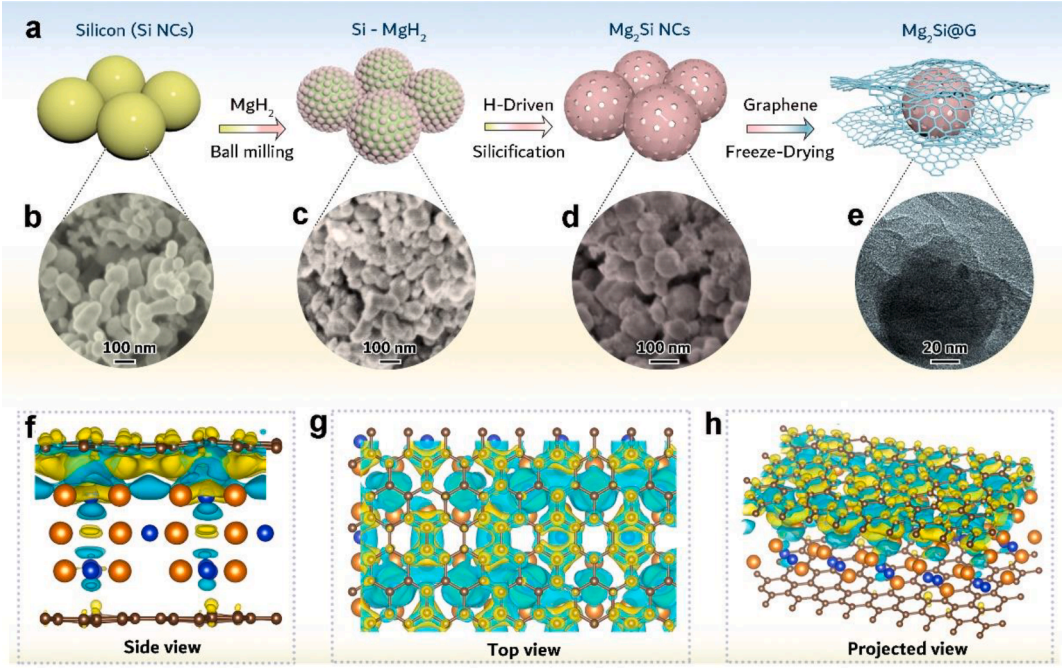

Fig. 1. (a) Schematic illustration of the preparation of Mg_2Si NCs and Mg_2Si@G. The corresponding SEM images of (b) Silicon, (c) the well dispersed Si-MgH_2 mixture, (d) the obtained Mg_2Si NCs, and (e) the final product of Mg_2Si@G. (f) Side, (g) top, and (h) projected views of the charge density difference map of Mg_2Si@G. Skyblue and yellow regions display the isosurfaces of electron depletion and accumulation.

matrix (Fig. 1e) based on molecular interactions during freeze drying process, resulting in Mg_2Si@G with high loading content (75.0 wt%). Additionally, based on the density functional theory (DFT) calculations, the Mg_2Si@G shows a favorable binding energy of −0.074 eV per formula of Mg_2Si between Mg_2Si and graphene. The calculated charge density difference map (Fig. 1f–h) displays clear electron transfer between graphene and Mg_2Si. As shown, there is a positive electron accumulation between graphene and Mg atoms, and a negative charge region between bottom Si atoms and graphene can be found. Overall, there are small charge isosurfaces in the Mg_2Si layer resulting from the charge redistribution between Mg_2Si with graphene. The interactions between graphene and Mg_2Si assures the confinement of graphene on Mg_2Si, leading to favorable structure of Mg_2Si@G for stable lithium storage.

The crystallographic structures were identified by the powder X-ray diffraction (PXRD). Fig. 2a shows that the active process based on ball milling process generates no new phases. After the H-driven reaction, all the diffraction peaks of the obtained samples (Fig. 2b) can be well indexed to Mg_2Si FCC cubic anti-fluorite-type structure (JCPDS no. 65-2988), indicating that pure Mg_2Si phase can be synthesized. On the contrary, there are always some impurity peaks related to MgO in the commercial Mg_2Si bulks as shown in the cycle of Fig. 2b. Moreover, the peak intensity ratio $I_{(111)}/I_{(220)}$ for the obtained Mg_2Si NCs is calculated to be 0.27, which is much smaller than that of commercial Mg_2Si bulk (0.38) and the reference data (0.41), indicating a preferential growth of (220) planes. It can further be verified by the similar trends in other $I_{(200)}/I_{(220)}$, $I_{(311)}/I_{(220)}$, and $I_{(400)}/I_{(220)}$ intensity ratios of Mg_2Si NCs and the standard values (Table S1). Generally, the difference in a certain peak intensity suggests a preferred orientation along a particular facet, relating to the surface energy [42–44]. DFT calculations show that the (220) planes have the lowest energy (0.0129 J m^{-2}) of different facets, indicating a much stable surface. Besides, the X-ray photoelectron spectroscopy (XPS) of Mg_2Si@G (Fig. S1) further reveals the presence of Mg, Si and C in the surface composition. The corresponding high-resolution XPS in Fig. 2c, d displays the characteristic peaks of Si 2p3 spectrum (103.6 eV) and Mg 2p spectrum (51.1 eV), verifying the formation and interaction of Mg_2Si@G. The corresponding C1s spectrum (Fig. 2e) demonstrates the characteristic peak (284.8 eV) related to the graphene, as well as the shoulder peak at 286.8 eV, which is ascribed to the favorable interactions between Mg_2Si and graphene predicated in the DFT calculation. Note that there is also part of MgO and Mg $(OH)_2$ detected in the sample due to the inevitable exposure of sample during test to air.

The morphology and structure of samples were characterized by FE-SEM and FE-TEM. According to Fig. 3a–c, Mg_2Si NCs exhibits an average particle size of 50 nm, which are in good morphology-inheritance with the initial Silicon and the Si-MgH_2 intermediate sample (Fig. S2). A series of nanopores resulting from the surface diffusion and coarsening accompanied with the dehydrogenation of MgH_2 during the silicification, are uniformly dispersed on Mg_2Si NCs (Inset of Fig. 3c and S3). This consists well with the pores distribution further as verified by the absorption-desorption test (Fig. S4), which demonstrates the type II nitrogen isotherm with average pore volume of 1.27 nm. The nanocrystals in the HRTEM image (Fig. 3d) clearly displays the lattice fringes of 2.24 and 3.66 Å, relating to (220) and (111) planes of Mg_2Si, respectively. In addition, the EDS elemental mapping of Si and Mg shows almost overlapped distribution with a molar ratio close to 2:1 (Fig. 3e), further verifying the complete formation of Mg_2Si. Fig. 3f–h displays the Mg_2Si NCs encapsulated by flexible graphene-layer matrix (Mg_2Si@G) after freeze-drying treatment. The HRTEM images (Fig. 3i, j) show that the characteristic (220) and (111) planes of Mg_2Si NCs are well encapsulated by the graphene lattices. The corresponding cystalline oritation was shown in the FFT pattern (Fig. 3k). In addition, the EDS elemental mapping images of C, Mg and Si (Fig. 3l) further verify the homogeneous distribution of Mg_2Si NCs on graphene. The Mg_2Si@G could ensure efficient electron conduction and spatially confinement,

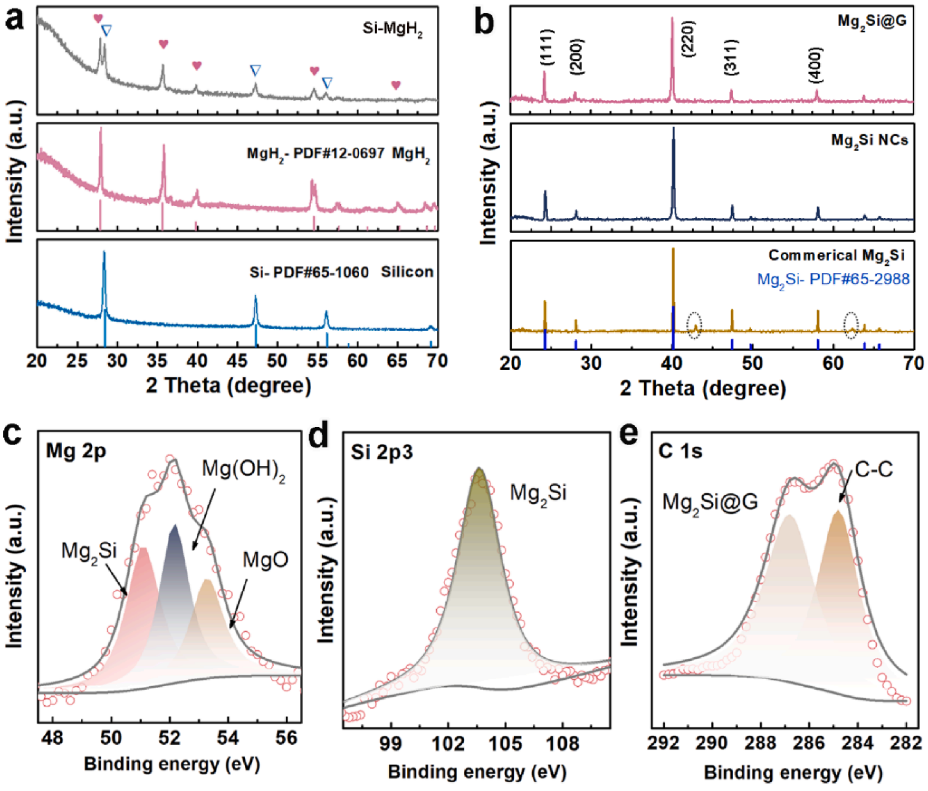

Fig. 2. (a) PXRD patterns of raw materials (Silicon and MgH_2), and the intermediate sample after ball milling treatment (Si-MgH_2). (b) PXRD pattern of the commercial Mg_2Si sample, the as-synthesized Mg_2Si NCs and Mg_2Si@G samples, λ = 1.5406. The cycles in the commercial Mg_2Si sample are indexed to the impurity of MgO. (c) The high-resolution XPS spectra of (c) Mg 2p, (d) Si 2p3 and (e) C 1s for Mg_2Si@G.

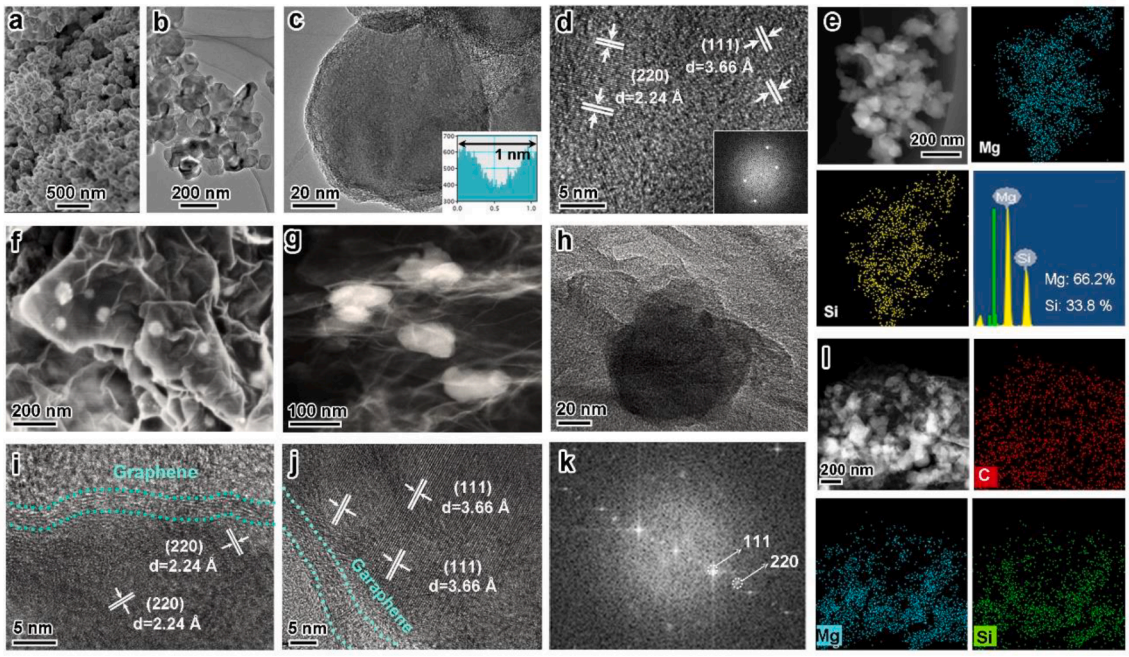

Fig. 3. Morphologies of the as-synthesized Mg_2Si NCs and Mg_2Si@G. (a) SEM image, (b, c) TEM images, and (d) HRTEM image of Mg_2Si NCs. Inset of (c) is the size of the nanopores. Inset of (d) is the corresponding FFT pattern. (e) The elemental mapping images of Mg and Si of Mg_2Si NCs and corresponding EDS spectrum. (f) SEM image, (g) STEM image, (h) TEM image, (i–k) HRTEM images and corresponding FFT pattern of Mg_2Si@G. (l) The elemental mapping images of C, Mg and Si of Mg_2Si@G.

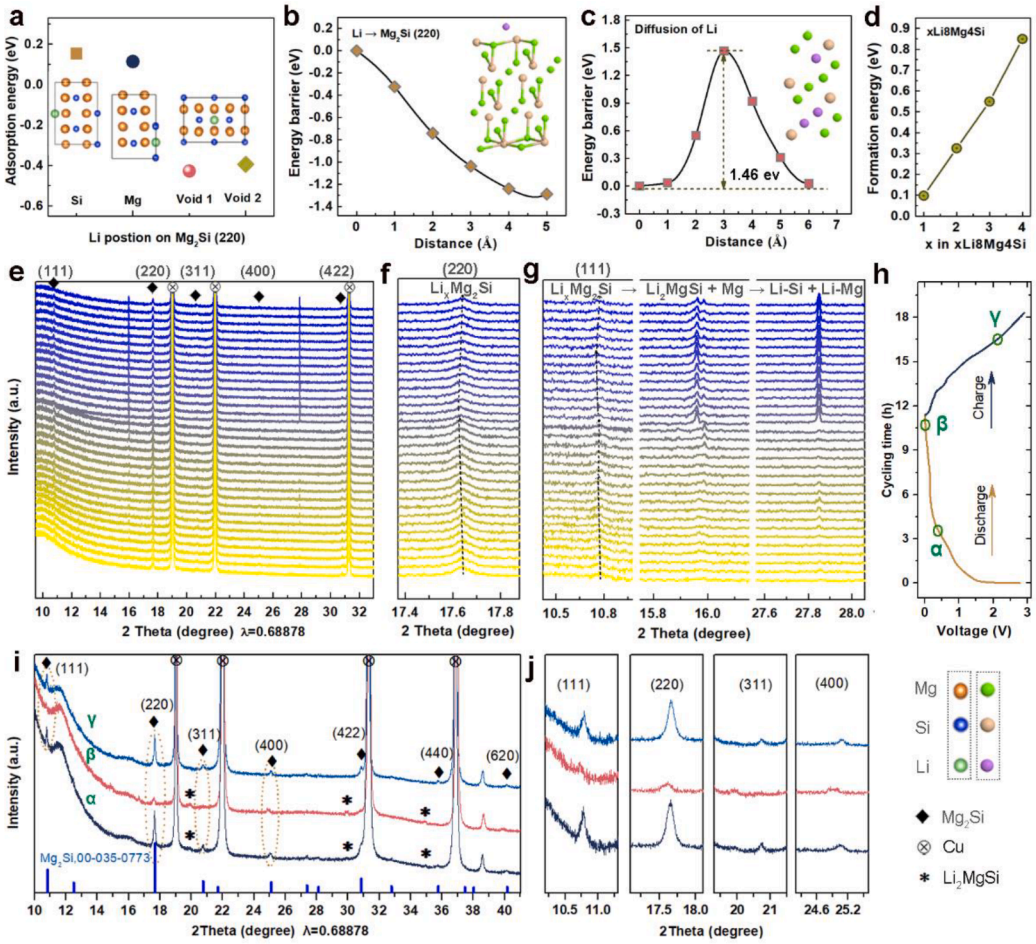

Fig. 4. (a) Adsorption energy of Li-ions onto different positions of Mg_2Si (220) surface. (b) Energy barrier and pathways for Li-ions approaching Mg_2Si (220). (c) Energy barrier and the pathways for Li-ions migration of in structure of Mg_2Si. (d) Formation energy of different percentage of Li insertion into Mg_2Si. (e) *In operando* synchrotron PXRD patterns of a Mg_2Si@G cycling battery, (f–h) the typical Bragg peaks, and (i) the corresponding discharge and charge voltage curves. (j) *Ex situ* PXRD patterns of Mg_2Si@G electrode cycled at different voltages (α, β, and γ) after a heat treatment and (k) the corresponding enlarged Bragg peaks.

which will certainly enhance the overall electrochemical activity and improve the structural stability. As a comparison, the commercial Mg_2Si exhibits bulk particles with severe aggregation even after ball milling (Fig. S5).

2.2. Anisotropic lithium storage behavior of Mg_2Si@G

To illustrate the lithium storage behavior of Mg_2Si, DFT calculation and modelling based on the high exposed (220) planes were carried out. According to the Eqs. ((1)–(3)), it could be deduced that Li-ions in the electrolyte would first adsorb onto Mg_2Si, and then intercalate and substitute into Mg_2Si structure. Fig. 4a displays the adsorption energy for four possible adsorption sites of Li-ions onto Mg_2Si (220). It shows that Li-ions adsorb onto Si atoms and Mg atoms are energy unfavorable with the adsorption energy of 0.15 and 0.11 eV, respectively; while Li preferentially adsorb onto void space above 2 Mg and 2Si with different initial heights, forming strong chemical bonding with negative adsorption energies (−0.42 eV and −0.39 eV, respectively). Therefore, the favorable positions for Li-ions adsorption onto Mg_2Si are above voids of (220) surface. Furthermore, calculations based on the Climbing Image Nudged Elastic Band (CINEB) method were performed to illustrate the energy barrier for the migration path of Li-ions. According to Fig. 4b, the closer Li-ions approach to the Mg_2Si surface, the lower energy barrier it will be. It indicates an energy favorable diffusion path for Li-ions to absorb onto Mg_2Si surface. Fig. 4c further shows the void-to-void diffusion of Li-ions in structure of Mg_2Si, which exhibits one saddle point with an energy barrier of 1.46 eV at a distance of round 6.3 Å, indicating an efficient Li-ions migration path along high exposed (220) facets.

$$Mg_2Si + xLi^+ + xe^- \leftrightarrow Li_xMg_2Si,\ 0 \le x \le 1 \quad (1)$$

$$Li_xMg_2Si + yLi^+ + ye^- \leftrightarrow Li_2MgSi + Mg \leftrightarrow \text{Li-Si Alloy} + Mg,\ x + y \ge 2 \quad (2)$$

$$Mg + zLi^+ + ze^- \leftrightarrow \text{Li-Mg Alloy},\ z \ge 0 \quad (3)$$

Additionally, the max number of Li-ions insertion into the interstitial sites of Mg_2Si was calculated, based on the solid solution behavior for one-unit cell (xLi + 8Mg4Si → xLi8Mg4Si). According to Fig. 4d, energy formation of xLi8Mg4Si increases as the percentage of Li-ions insertion increases, indicating an energy unfavorable. Then the alloying reaction of solid solution phase of Li_xMg_2Si tends to start a conversion reaction after a critical number of Li-ions been diffused into the crystal structure as in equations below. A full occupation of 4 Li could be inserted into interstitial position, contributing to 1 lithium capacity by forming a saturated solid solution $LiMg_2Si$. With higher Li insertion, Mg atoms could be further substituted or shared a mixed occupancy atomic position, leading to structural expansion and conversion.

The structural evolution of Mg_2Si@G during lithium storage was further elucidated by *in operando* synchrotron PXRD. As shown in Fig. 4e, these diffraction peaks relating to the characteristic (111), (220), (311), (400) and (422) planes of Mg_2Si NCs and the peaks from Cu (current collector) can be well identified. Upon discharging, the dominant diffraction peak (220) gradually shifts to low angle, along with peak broadening and intensity decreasing (Fig. 4f), indicating a solid solution behavior (Eq. (1)). During the charge process, the peaks could recover correspondingly, suggestive of a good structural stability of (220) planes and highly reversible Li diffusion. This solid solution behavior is consistent well the DFT calculations aforementioned and can also be verified by the *ex-situ* PXRD patterns (Fig. S6). Except from the similar solid solution process, the diffraction peak of (111) gradually shifts to high angle with intensity decrease when discharging to low voltage (Fig. 4g), suggestive the further decomposition process due to more insertion of Li-ions substitute for Mg atoms (Eq. (2)). This process could be further verified by the transient of the new Bragg peaks at about 27.8°, which can be related to the lattice variation of intermediate phases e.g., Li_2MgSi. Correspondingly, the phase variation at the Bragg peak of 16° represents the emerging of Mg (101) and its further Li-Mg alloying during discharging (Eq. (3)). Note that due to the internal strain after lithium insertion and the poor crystallinity, part of the intermediates is amorphous (e.g., Li-Si alloy), which can't be detected in the XRPD patterns. Interestingly, the crystal lattices at 16.0° and 27.8° demonstrate enhanced intensity during the charge process, which could be largely ascribed to the structural arrangement during Li extraction process. As a result, part of the intermediate phases is likely to participate in the following cycling as part of the active materials. Additionally, Mg_2Si@G electrodes at different cycling stages (Fig. 4h) were subjected to a heat treatment (100 °C) under vacuum to be better crystallized. Fig. 4i and j show that the PXRD patterns of Mg_2Si@G are at typical voltage stages (α, β, and γ), which display much better crystallization and further confirm the reversible (de)lithiation process.

2.3. Enabled battery performance of Mg_2Si@G electrode

Fig. 5a shows the cyclic voltammetry (CV) curves of Mg_2Si@G. In the first cathodic scan, the broad peak centered at 0.68 V can be related to the irreversible formation of SEI films layer alone with the generation of Li_xMg_2Si solid solution (Eq. (1)). The consistent cathodic peaks range from 0.18 V to 0.10 V correspond to the consistent insertion of Li to substitute for Mg atoms (Li_2MgSi) along with the formation of Li-Si alloy (Eq. (2)). The sharp peak at about 0.005 V relates to the further Li-Mg alloying (Eq. (3)). It is noted that due to the complicated mechanism of Mg_2Si, the above lithiation processes might be overlapped or happened in parallel. Correspondingly, there were three apparent peaks in the anodic scan, respectively. The peak at about 0.2 V corresponds to the de-alloying process of Li-Mg alloy, followed by the delithiaiton of Li_2MgSi and Li-Si phases at 0.3 V. The broad peak centered at 0.65 V further verifies the reformation of Mg_2Si. Similar cathodic/anodic peaks can be well detected at the same position in the following cycles. Note that Eqs. ((1)–(3)) exhibits that Mg_2Si electrode suffer from a volumetric expansion-shrinkage-expansion process during the cycling, leading to part of evitable irreversibility. The CV profiles of Mg_2Si@G are in good consistent with the Mg_2Si NCs electrode, both of which show much better electrochemical activity and stability than the commercial Mg_2Si (Fig. S7). According to Fig. 5b, the discharge-charge voltage profiles of Mg_2Si@G display pairs of discharge-charge plateaus, the voltages of which agree well with the obtained CV results.

The galvanostatic charge/discharge performances of Mg_2Si@G, Mg_2Si NCs, commercial Mg_2Si, and graphene were tested at a current rate of 100 mA g^{-1} for comparison. The specific capacities were tested by the weight of active materials. As shown in Fig. 5c, the initial discharge capacity of the commercial Mg_2Si is 1980 mAh g^{-1}, but the capacity decays fast to 475 mAh g^{-1} and 280 mAh g^{-1} after 20 and 50 cycles, respectively. In comparison, the Mg_2Si NCs electrode displays a much higher initial discharge capacity of 2244 mAh g^{-1}, but it also comes across a fast decay, with a capacity of 580 mAh g^{-1} after 50 cycles. Moreover, Mg_2Si@G electrode delivers an initial discharge/charge capacities of 2739 mAh g^{-1} and 1624 mAh g^{-1}, respectively. The high initial capacity can be mainly ascribed to the inevitable generation of irreversible SEI films, the conversion-alloying lithiation process, as well as the capacitive capacity contribution especially at the present of graphene. After the 2nd and 3rd cycling, the Coulombic efficiency increased to 90.4% and 92.8%, indicating a more stable SEI layer. It is highly expected that with more future endeavor, the initial Coulombic efficiency of this kind of materials could be further optimized for practical application. Over 100 cycles, it still retains a high reversible capacity of 831 mAh g^{-1} and displays a Coulombic efficiency of 94.4%. Note that pure graphene electrode delivers a low discharge capacity of 300 mAh g^{-1} (Fig. S8), and thus its capacity contribution on Mg_2Si@G could be neglected in long cycles.

Besides, Mg_2Si@G electrode demonstrates outstanding rate capability. As shown in Fig. 5d, when cycled at various current densities of 100, 200, 500, 1000 and 2000 mA g^{-1}, Mg_2Si@G anode delivers high

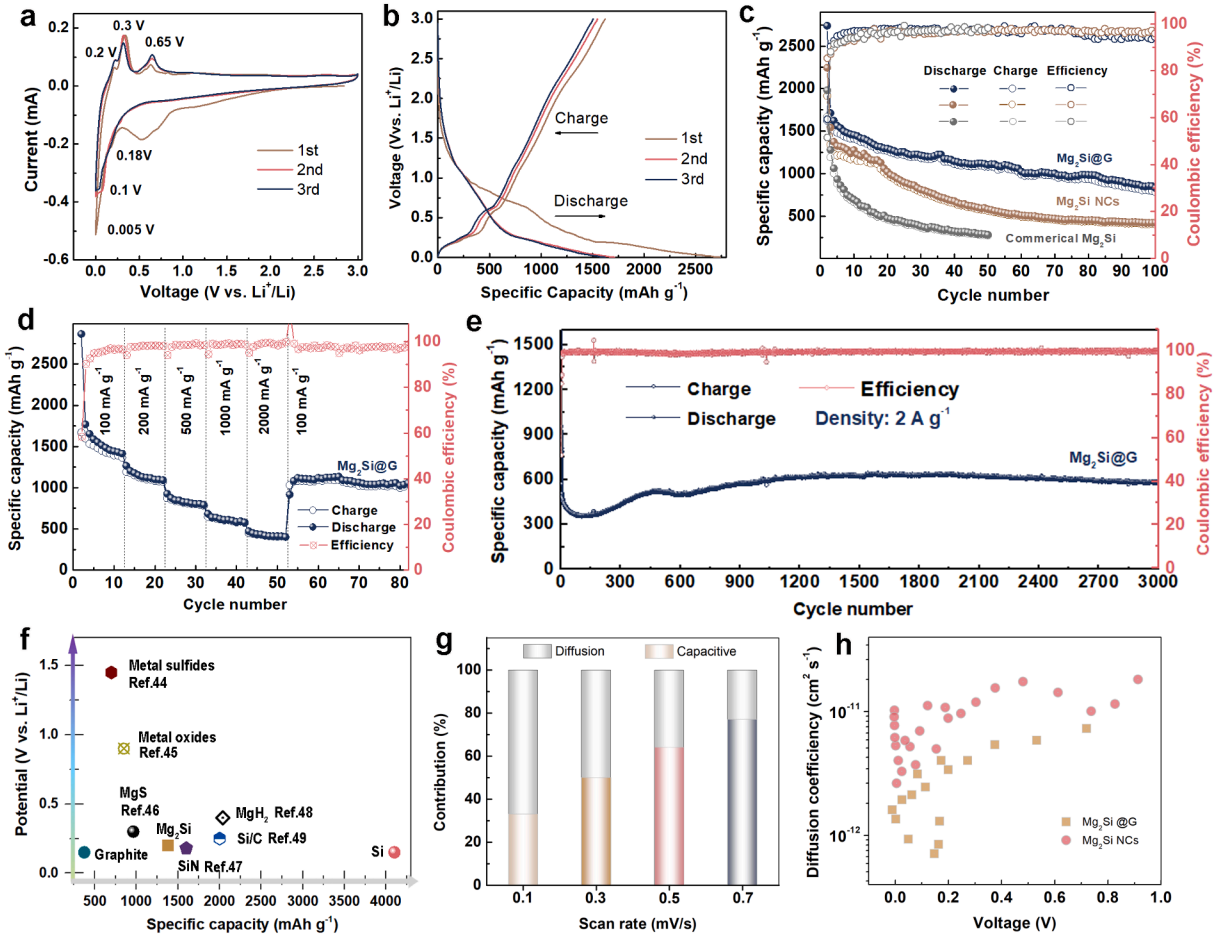

Fig. 5. (a) Cyclic voltammetry curves of Mg_2Si@G electrode at 0.1 mV s^{-1}. (b) Discharge-charge voltage profiles of Mg_2Si@G at a rate of 100 mA g^{-1}. (c) Cycling performances of Mg_2Si@G, Mg_2Si NCs, and commercial Mg_2Si electrodes at a current density of 100 mA g^{-1}. (d) Rate capabilities of Mg_2Si@G. (e) Cycling stability of Mg_2Si@G at a high current density of 2 A g^{-1}. (f) Comparison of the theoretical capacities and potentials of widely reported electrodes for LIBs. (g) The normalized contribution ratio at different scan rates. (h) The calculated Li-ion diffusion coefficient in at different charge–discharge stages.

reversible capacities of 1515, 1130, 809, 613, and 418 mAh g^{-1}, respectively. As the current rate reduces to 100 mAh g^{-1}, the corresponding capacity recovers to 1083 mAh g^{-1}. Furthermore, Mg_2Si@G electrode exhibits outstanding long-time stability when cycled at a high current rate. According to Fig. 5e, a high 3000th capacity of 578 mAh g^{-1} still maintains when cycled at 2 A g^{-1}, with a Coulombic efficiency of 99.7%. Noting that the slightly increased capacity during cycling is mainly ascribed to the activation process of Mg_2Si nanocrystals caused by the repeated (de)lithiation process and the capacitive lithium-storage behavior at high cycling rate. To the best of our knowledge, it is the best reported performance of Mg_2Si-based materials, which largely exceeds to that of commercial graphite electrode (372 mAh g^{-1}) for LIBs. When compared with these widely reported electrode materials for LIBs, Mg_2Si-based materials also outperform most of the metal-based materials and are comparable to these Mg- and Si-based electrodes (Fig. 5f) [45–50]. The outstanding performance is largely attributed to the unique structure of uniform Mg_2Si NCs with nanopores, which not only improve the diffusion kinetics by shorting the Li-ions/electron transport path and promoting electrolyte transport, but also alleviate the volumetric effect by providing volume-containable space during cycling, contributing to enabled lithium storage performance.

2.4. *Structural superiority and interactions of Mg_2Si@G*

To further elucidate the electrochemical kinetics of Mg_2Si@G, different CV profiles at stepped scan rates from 0.1 to 0.7 mV s^{-1} were tested (Fig. S9). In our case, the adjustable parameters *b* of the representative peak is determined to be 0.58, indicating the co-existence of diffusion-controlled process and capacitive behavior [47]. As shown in Fig. 5g, Mg_2Si@G electrdoe displays about 33% capacitive contribution on capacity at a scan rate of 0.1 mV s^{-1}, suggesting that the diffusion process dominated process. With the increase of a scan rates, the capacitive contribution would gradually increase, mainly ascribing to the present of large number of active sites on/near the surface areas generated in the pore-engineered nanoarchitecture. Besides, the galvanostatic intermittent titration technique (GITT) was also carried out to examine the dynamics of Li^+ diffusion of Mg_2Si@G electrode [51]. According to the calculated electrodes Li^+ diffusion coefficient (D_{Li+}) as shown in Figs. 5h and S10, the order of magnitude of D_{Li+} for Mg_2Si@G in the discharge processes is between 10^{-11} and 10^{-12}, which is much higher than that of Mg_2Si NCs. As the result, the fast Li^+ transport contributes to enhanced electrochemical performance.

In addition, electrochemical impedance spectroscopy (EIS) was conducted to illustrate the electrical conductivity, the charge transfer resistance, and ion diffusion kinetics at the interface of electrolyte/electrode. As shown in Fig. S11, the Nyquist plots of Mg_2Si based electrodes consist of a depressed semicircle at the range of medium-to-high frequencies, and a subsequent straight line with certain slope in the range of low frequencies. According to the equivalent circuit (inset of Fig. S11), the obtained R_S, R_{CT}, and W_o correspond to the resistances of SEI layer, the charge-transfer resistances, and the Warburg impedance is related to the Li-ions diffusion, respectively. According to the fitting

results, the corresponding R_{CT} values for Mg_2Si@G, Mg_2Si NCs, and commercial Mg_2Si electrodes are calculated to be 87.3 Ω, 156.5 Ω and 177.0 Ω, respectively. The obtained smallest depressed semicircle of Mg_2Si@G electrode at the range of middle-high frequency indicates a higher overall electronic conductivity and lower charge transfer resistance, by virtue of the graphene coating layer and highly exposed (220) facets.

The Li-driven structural evolution and stability of Mg_2Si@G electrode upon cycling was studied by TEM. After the first lithiation process (Fig. 6a), Mg_2Si NCs electrode still maintains its initial stable nanostructure characterized with the active materials encapsulated by graphene. Fig. 6b displays a variety of lattice fringes ranging from 2.18 to 2.65 Å, which can be mainly ascribed to the lattice changes of the (220) and (111) planes of Mg_2Si during the Li insertion, resulting in multiple nanocrystalline phases. These results are also in good accordance with the PXRD observation. Moreover, Mg_2Si@G demonstrates an excellent structural integrity even after long-term cycles at a high current rate (Fig. S12). The corresponding STEM image as well as EDS elemental mapping of C, Mg, and Si of Mg_2Si@G electrode after cycling display a uniform distribution (Fig. 6c) under the confinement of graphene. On the contrary, the pure Mg_2Si NCs without graphene suffers from server agglomeration and pulverization after cycling (Fig. S13), leading to fast capacity fading after 20 cycles. The well-sustained structural stability of Mg_2Si@G during cycling is also largely attributed to the confinement of graphene onto Mg_2Si NCs at nanoscale (Fig. 6d), which could largely alleviate the volumetric effect the (de)lithiation process, prevent the pulverization and detachment of active materials, assuring a long-term stability.

Expect the spatially confined effect, the interactions derived between absorbed Li-ions and Mg_2Si@G (Mg_2Si@G + Li) are beneficial for lithium storage behavior. According to Figs. 6e and S14, the electronic structure of Mg_2Si@G + Li system analyzed by the Valence electron localization function (VELF) shows that there are highly localized electrons between Mg and Si atoms with maximum closer to Si atom, suggesting an ionic bonding interactions between Mg-Si. Based on the low VELF value between graphene layer and Mg_2Si, the interfaces are dominated by the Van der Waals interactions. It also represents the physisorption of Li-ions on Mg_2Si surface based on the VELF minimum between Mg_2Si layers and Li-ions. Moreover, the density of states (DOS) shows that the Mg_2Si@G + Li system displays a metallic feature, with a high value of local states across the Fermi level (Fig. 6f). It can be attributed to the hybridized orbitals of C, Mg, and Si atoms and the charge redistribution among Mg_2Si, Li, and graphene, which changes the electron density near Fermi level though. This phenomenon could also be illustrated by the charge density difference map of Mg_2Si@G + Li system (Fig. 6g). As shown, charges accumulate at the interface between Li-ions and graphene, and the interface between Mg_2Si slab and graphene layer. Meanwhile, the regions of charge depletion appear within Mg_2Si slab and near the top of Li. This suggests that a built-in electric field directed from Li-ions to Mg_2Si could generate, resulting from the charge flow Li to graphene and then to Mg_2Si layers. As an efficient electron collector, graphene could largely enhance the electron transfer within Mg_2Si structure, which largely contributes to enhanced electrochemical kinetic during lithium storage process.

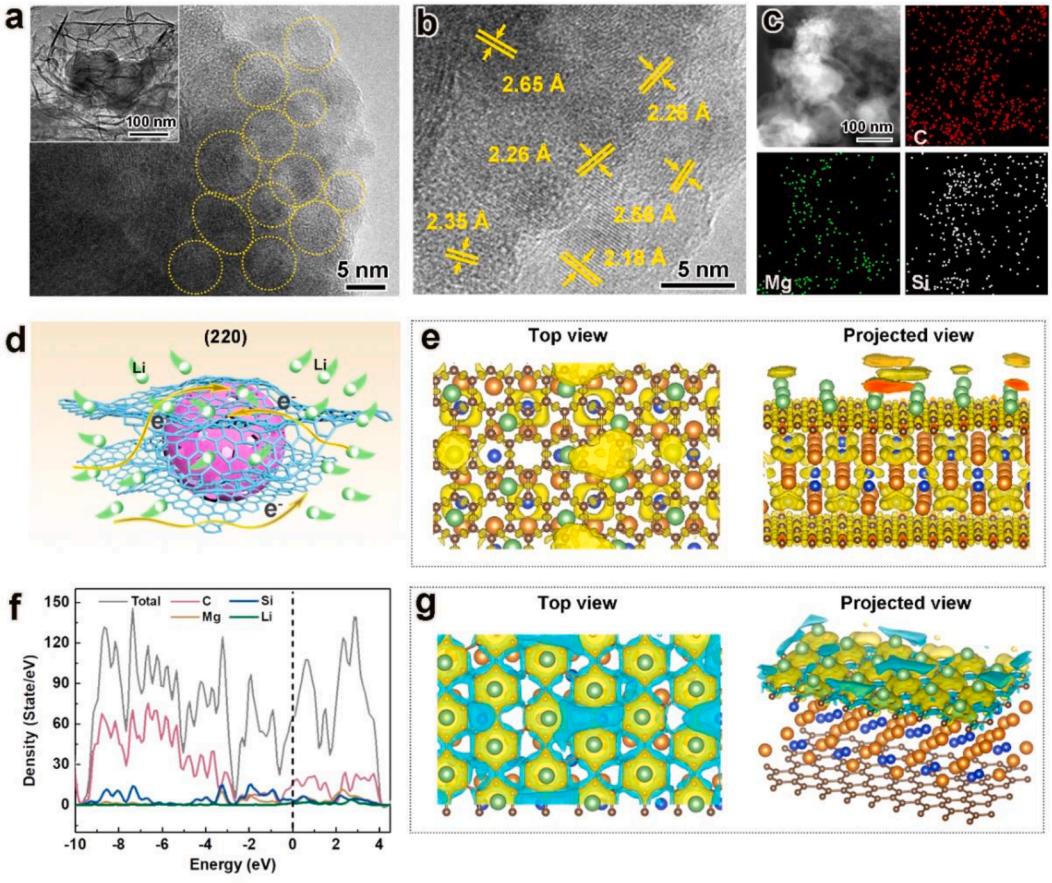

Fig. 6. (a) TEM images, (b) HRTEM image of Mg_2Si@G electrode after the first lithiation state. (c) STEM image and the elemental mapping of Mg_2Si@G at high density of 200 mA g^{-1} over 100 cycles. (d) Schematic illustration of the (de)lithiation behavior of Mg_2Si@G. (e) Top and projected views of valence electron localization functions (VELF) of Li + Mg_2Si@G. (f) The calculated Density of States (DOS) of Li + Mg_2Si@G. (g) Top and side view of charge density difference map of Li + Mg_2Si @G. Skyblue and yellow regions correspond to isosurface of electron depletion and accumulation.

3. Conclusion

In summary, we report a graphene confined Mg_2Si with highly exposed (220) facets and nanoporous structure, and its advanced lithium storage performance. The intermetallic Mg_2Si@G was fabricated based on a facile hydrogen-driven silicification, involving the dehydrogenation of MgH_2, the lattice orientation rearrangement, and Mg_2Si nanocrystals growth, followed by a freeze-drying process. When evaluated as electrode materials for LIBs, Mg_2Si@G exhibits high-capacity utilization, fast electronic/ionic transport kinetics, and well-sustained stability. The enhancement of electrochemical properties is mainly attributed to the structural features of Mg_2Si@G and the rapid Li-ions migration path along exposed (220) facets, which assures a spatially confined (de)lithiation process and solid solution behavior with high reversibility. As a result, Mg_2Si@G electrode delivers a high capacity of 831 mAh g^{-1} at 100 mA g^{-1}, outstanding rate capability, and excellent long-term cycle stability with a 3000th capacity of 578 mAh g^{-1} at 2 A g^{-1}. Overall, this work presents a rational and effective design towards the exploration of well-performing Mg_2Si electrode materials for LIBs. Also, it is believed that the research perspective on crystallographic planes orientation could also shed new light on rational design of Si-M intermetallic and related nanomaterials in numerous applications.

Declaration of Competing Interest

The authors declare that they have no known competing financial interests or personal relationships that could have appeared to influence the work reported in this paper.

Acknowledgements

This work was partially supported by the National Science Fund for Distinguished Young Scholars (51625102), the National Natural Science Foundation of China (51971065), the Innovation Program of Shanghai Municipal Education Commission (2019-01-07-00-07-E00028), and the Science and Technology Commission of Shanghai Municipality (17XD1400700). Part of the experiment was performed at PD beamline, Australian Synchrotron, ANSTO. DFT calculation was conducted on ASCI.

Appendix A. Supplementary data

Supplementary data to this article can be found online at https://doi.org/10.1016/j.cej.2021.129660.

References

[1] W. Li, B. Song, A. Manthiram, High-voltage positive electrode materials for lithium-ion batteries, Chem. Soc. Rev. 46 (2017) 3006–3059.
[2] J.W. Choi, D. Aurbach, Promise and reality of post-lithium-ion batteries with high energy densities, Nat. Rev. Mater. 1 (2016) 16013.
[3] M.R. Lukatskaya, B. Dunn, Y. Gogotsi, Multidimensional materials and device architectures for future hybrid energy storage, Nat. Commun. 7 (2016) 12647.
[4] S. Chae, S.-H. Choi, N. Kim, J. Sung, J. Cho, Integration of graphite and silicon anodes for the commercialization of high-energy lithium-ion batteries, Angew. Chem. 59 (2020) 110–135.
[5] G. Ziegenbalg, T. Focke, H. Holldorf, R. Brink, H. Lange, Gas-phase synthesis of amorphous silicon nitride-reaction paths and powder characteristics, J. Mater. Sci. 34 (1990) 2199–2206.
[6] S. Li, J. Niu, Y.C. Zhao, K.P. So, C. Wang, C.A. Wang, J. Li, High-rate aluminium yolk-shell nanoparticle anode for Li-ion battery with long cycle life and ultrahigh capacity, Nat. Commun. 6 (2015) 7872.
[7] Y. Oumellal, A. Rougier, G.A. Nazri, J.-M. Tarascon, L. Aymard, Metal hydrides for lithium-ion batteries, Nat. Mater. 7 (2008) 916–921.
[8] M. Sun, H. Liu, J. Qu, J. Li, Earth-rich transition metal phosphide for energy conversion and storage, Adv. Energy Mater. 6 (2016) 1600087.
[9] D.H. Youn, S.K. Stauffer, P. Xiao, H. Park, Y. Nam, A. Dolocan, G. Henkelman, A. Heller, C.B. Mullins, Simple synthesis of nanocrystalline tin sulfide/N-doped reduced graphene oxide composites as lithium-ion battery anodes, ACS Nano 10 (2016) 10778–10788.
[10] Y. Zhong, X. Xia, F. Shi, J. Zhan, J. Tu, H.J. Fan, Transition metal carbides and nitrides in energy storage and conversion, Adv. Sci. 3 (2016) 1500286.
[11] X. Xu, W. Liu, Y. Kim, J. Cho, Nanostructured transition metal sulfides for lithium-ion batteries: progress and challenges, Nano Today 9 (2014) 604–630.
[12] G.A. Li, C.Y. Wang, W.C. Chang, H.Y. Tuan, Phosphorus-rich copper phosphide nanowires for field-effect transistors and lithium-ion batteries, ACS Nano 10 (2016) 8632–8644.
[13] R.A. Huggins, A.A. Anani, Metal Silicide Electrode in Lithium Cells, US Patent, 1990.
[14] H. Jia, C. Stock, R. Kloepsch, X. He, J.P. Badillo, O. Fromm, B. Vortmann, M. Winter, T. Placke, Facile synthesis and lithium storage properties of a porous $NiSi_2$/Si/carbon composite anode material for lithium-ion batteries, ACS Appl. Mater. Interfaces 7 (2015) 1508–1515.
[15] L. Deng, Y. Cui, J. Chen, J. Wu, A.P. Baker, Z. Li, X. Zhang, A core-shell Si@$NiSi_2$/Ni/C nanocomposite as an anode material for lithium-ion batteries, Electrochim. Acta 192 (2016) 303–309.
[16] D. Zhou, H. Jia, J. Rana, T. Placke, R. Klöpsch, G. Schumacher, M. Winter, J. Banhart, Investigation of a porous $NiSi_2$/Si composite anode material used for lithium-ion batteries by X-ray absorption spectroscopy, J. Power Sources 324 (2016) 830–835.
[17] Y. Chen, J. Qian, Y. Cao, H. Yang, X. Ai, Green synthesis and stable li-storage performance of $FeSi_2$/Si@C nanocomposite for lithium-ion batteries, ACS Appl. Mater. Interfaces 4 (2012) 3753–3758.
[18] H.Y. Lee, S.M. Lee, Graphite–FeSi alloy composites as anode materials for rechargeable lithium batteries, J. Power Source 112 (2002) 649–654.
[19] S. Zhou, X. Liu, D. Wang, Si/$TiSi_2$ Heteronanostructures as high-capacity anode material for li ion batteries, Nano Lett. 10 (2010) 860–863.
[20] M.S. Shin, T.W. Lee, J.B. Park, S.H. Lim, S.M. Lee, Post-annealing effects on the electrochemical performance of a Si/$TiSi_2$ heteronano structured anode material prepared by mechanical alloying, J. Power Source 344 (2017) 152–159.
[21] F.M. Courtel, D. Duguay, Y. Abu-Lebdeh, I.J. Davidson, Investigation of $CrSi_2$ and $MoSi_2$ as anode materials for lithium-ion batteries, J. Power Source 202 (2012) 269–275.
[22] L. Wu, J. Yang, X. Zhou, J. Tang, Y. Ren, Y. Nie, Enhanced electrochemical performance of heterogeneous Si/$MoSi_2$ anodes prepared by a magnesiothermic reduction, ACS Appl. Mater. Interfaces 8 (2016) 16862–16868.
[23] H.L.T. Feng, Q.G. Fu, X. Yang, H. Wu, High-temperature erosion resistance and aerodynamic oxidation mechanism of multi-layer $MoSi_2$-$CrSi_2$-Si/SiC coated carbon/carbon composites in a wind tunnel at 1873 K, Carbon 50 (2012) 2171–2178.
[24] J. Wolfenstine, $CaSi_2$ as an anode for lithium-ion batteries, J. Power Sources 124 (2003) 241–245.
[25] K. Sasidharachari, S. Yoon, Electrochemical performance of $CaSi_2$-C composite as an anode material for lithium-ion batteries, Int. J. Appl. Eng. Res. 11 (2016) 7284–7287.
[26] C. Xiao, N. Du, H. Zhang, D. Yang, Improved cyclic stability of Mg_2Si by direct carbon coating as anode materials for lithium-ion batteries, J. Alloy. Compd. 587 (2014) 807–811.
[27] H. Kim, J. Choi, H.J. Sohn, T. Kang, The insertion mechanism of lithium into Mg_2Si anode material for Li-ion batteries, J. Electrochem. Soc. 146 (1999) 4401–4405.
[28] R. Ma, Y. Liu, Y. Yang, M. Gao, H. Pan, Mg_2Si anode for Li-ion batteries: linking structural change to fast capacity fading, Appl. Phys. Lett. 105 (2014) 652.
[29] S.W. Song, K.A. Striebel, R.P. Reade, G.A. Roberts, E.J. Cairns, Electrochemical studies of nanoncrystalline Mg_2Si thin film electrodes prepared by pulsed laser deposition, J. Electrochem. Soc. 150 (2002) A121–A127.
[30] S.W. Song, K.A. Striebel, X. Song, E.J. Cairns, Amorphous and nanocrystalline Mg_2Si thin-film electrodes, J. Power Sources 119 (2003) 110–112.
[31] N.S. Nazer, R.V. Denys, H.F. Andersen, L. Arnberg, V.A. Yartys, Nanostructured magnesium silicide Mg_2Si and its electrochemical performance as an anode of a lithium-ion battery, J. Alloy. Compd. 718 (2017) 478–491.
[32] A.G. Tamirat, M. Hou, Y. Liu, D. Bin, Y. Sun, L. Fan, Y. Wang, Y. Xia, Highly stable carbon coated Mg_2Si intermetallic nanoparticles for lithium-ion battery anode, J. Power Sources 384 (2018) 10–17.
[33] J.M. Yan, H.Z. Huang, J. Zhang, Y. Yang, The study of Mg_2Si/carbon composites as anode materials for lithium-ion batteries, J. Power Sources 175 (2008) 547–552.
[34] Y. Liu, Y. He, R. Ma, M. Gao, H. Pan, Improved lithium storage properties of Mg_2Si anode material synthesized by hydrogen-driven chemical reaction, Electrochem. Commun. 25 (2012) 15–18.
[35] Y. Liu, R. Ma, Y. He, M. Gao, H. Pan, Synthesis, structure transformation, and electrochemical properties of Li_2MgSi as a novel anode for Li-ion batteries, Adv. Funct. Mater. 24 (2014) 3944–3952.
[36] R. Ma, Y. Liu, Y. Yang, K. Pu, M. Gao, H. Pan, Li–Si-alloy-assisted improvement in the intrinsic cyclability of Mg_2Si as an anode material for Li-ion batteries, Acta Mater. 98 (2015) 128–134.
[37] P. Limthongkul, Y.I. Jang, N.J. Dudney, Y.M. Chiang, Electrochemically driven solid-state amorphization in lithium-silicon alloys and implications for lithium storage, Acta Mater. 51 (2003) 1103–1113.
[38] L. Wang, X.Y. Qin, W. Xiong, X.G. Zhu, Fabrication and mechanical properties of bulk nanocrystalline intermetallic Mg_2Si, Mater. Sci. Eng., A 459 (2007) 216–222.
[39] G.A. Roberts, E.J. Cairns, J.A. Reimer, Magnesium silicide as a negative electrode material for lithium-ion batteries, J. Power Sources 110 (2002) 424–429.
[40] B. Sun, S. Li, H. Imai, J. Umeda, K. Kondoh, Synthesis kinetics of Mg_2Si and solid-state formation of Mg-Mg_2Si composite, Powder Technol. 217 (2012) 157–162.
[41] E. Savary, F. Gascoin, S. Marinel, R. Heuguet, Spark plasma sintering of fine Mg_2Si particles, Powder Technol. 228 (2012) 295–300.
[42] L. Wang, X. He, W. Sun, J. Wang, Y. Li, S. Fan, Crystal orientation tuning of $LiFePO_4$ nanoplates for high-rate lithium battery cathode materials, Nano Lett. 12 (2012) 5632–5636.

[43] Z. Ding, D. Zhang, Y. Feng, F. Zhang, L. Chen, Y. Du, D.G. Ivey, W. Wei, Tuning anisotropic ion transport in mesocrystalline lithium orthosilicate nanostructures with preferentially exposed facets, NPG Asia Mater. 10 (2018) 606–617.
[44] L. Wang, J. Wan, Y. Zhao, N. Yang, D. Wang, Hollow multi-shelled structures of Co_3O_4 dodecahedron with unique crystal orientation for enhanced photocatalytic CO_2 reduction, J. Am. Chem. Soc. 141 (2019) 2238–2241.
[45] X.Y. Yu, L. Yu, X.W. Lou, Metal sulfide hollow nanostructures for electrochemical energy storage, Adv. Energy Mater. 6 (2016) 1501333.
[46] K. Cao, T. Jin, L.i. Yang, L. Jiao, Recent progress in conversion reaction metal oxide anodes for Li-ion batteries, Mater. Chem. Front. 1 (11) (2017) 2213–2242.
[47] B. Zhang, G. Xia, W. Chen, Q. Gu, D. Sun, X. Yu, Controlled-size hollow magnesium sulfide nanocrystals anchored on graphene for advanced lithium storage, ACS Nano 12 (2018) 12741–12750.
[48] S. Chae, S. Park, K. Ahn, G. Nam, T. Lee, J. Sung, N. Kim, J. Cho, A gas phase synthesis of amorphous silicon nitride nanoparticle for high-energy LIBs, Energy Environ. Sci. 13 (2020) 1212–1221.
[49] B. Zhang, G. Xia, D. Sun, F. Fang, X. Yu, Magnesium hydride nanoparticles self-assembled on graphene as anode material for high-performance lithium-ion batteries, ACS Nano 12 (2018) 3816–3824.
[50] Z. Xiao, C. Lei, C. Yu, X. Chen, Z. Zhu, H. Jiang, F. Wei, Si@Si_3N_4@C composite with egg-like structure as high-performance anode material for lithium-ion batteries, Energy Storage Mater. 24 (2020) 565–573.
[51] Z. Wu, C. Lu, Y. Wang, L. Zhang, L. Jiang, W. Tian, C. Cai, Q. Gu, Z. Sun, L. Hu, Ultrathin VSe_2 nanosheets with fast ion diffusion and robust structural stability for rechargeable zinc-ion battery cathode, Small 16 (2020) 2000698.